Journal of Stress Analysis
Vol. 4, No. 2, Autumn – Winter 2019-20
Bu-Ali Sina University

Static Analysis of Functionally Graded Piezoelectric Plates under Electro-thermo-mechanical Loading Using a Meshfree Method Based on RPIM

H. Nourmohammadi, B. Behjat*
Mechanical Engineering Faculty, Sahand University of Technology, Tabriz, Iran.

Article info

Article history:
Received 17 January 2020
Received in revised form
18 February 2020
Accepted 08 March 2020

Keywords:
Mesh-free methods
RPIM
FGPM
Electro-thermal loading

Abstract

In this paper, the static response of functionally graded piezoelectric plates under mechanical, electrical, and thermal loads is studied using a meshless method. The Radial Point Interpolation Method (RPIM) is used to create the shape function to approximate field variables. Given that RPIM shape functions pass Kronecker delta condition, boundary conditions can be applied directly. The First-order Shear Deformation Plate Theory (FSDT) is used to model the behavior of the plate. Power law distribution through the thickness is considered for all of mechanical, thermal, and piezoelectric properties. Effective parameters on deflection and stresses of Functionally Graded Piezoelectric Material (FGPM), including different electrical and mechanical loads, thermal loads, thickness, and different boundary conditions are studied. In this paper, the effect of power law index on the deflection and stresses of the functionally graded piezoelectric plate under external loads is investigated and different results are obtained in each case of mechanical, electrical, and thermal loading. By analyzing the results of this paper, the effective structure design and sensor/actuator behavior of the plate subjected to thermal and electrical loading could be obtained.

Nomenclature

$R_i(x)$	Radial basis function	Φ	Shape function matrix
$p_j(x)$	Polynomial basis function	L_x	Length of plate
b_j	Unknown coefficients of radial basis	L_y	Width of plate
a_i	Unknown coefficients of polynomial basis	nx	Number of nodes in x direction
n_s	Number of radial basis	ny	Number of nodes in y direction
m	Number of polynomial basis	α_c	Constant value that controls the value of C_d
q	MQ shape parameters	D_l	Electrical displacement
V_c	Volume fractions of top surface	C_{ijkl}	Elasticity tensor
V_m	Volume fractions of bottom surface	e_{lij}	Piezoelectric constant tensor
n	Power law index	θ	Temperature difference
h	Thickness of the plate	p_l	Pyroelectric vector
σ_{ij}	Stress tensor	k_{lk}	Dielectric permittivity coefficient tensor
ε_{kl}	Strain tensor	α_{kl}	Thermal expansion coefficient tensor

*Corresponding author: B. Behjat (Associate Professor)
E-mail address: behjat@sut.ac.ir
http://dx.doi.org/10.22084/jrstan.2020.20850.1125
ISSN: 2588-2597

Nomenclature

E_k	Electrical field	u_0, v_0, w_0	Displacement of mid-plane of plate
β_x	Rotation of transverse normal about y-axis	h_p	Thickness of the piezoelectric layer
β_y	Rotation of transverse normal about x-axis	$\vec{\tau}$	Surface tractions
R_ϕ	Electric field operator	$\vec{b}$	Body forces
φ	Shape function	λ_{ij}	Thermal expansion tensor
$u^h(x)$	Approximate function	R_Q	Radial moment matrix
C_d	Spacing between the nodes		

1. Introduction

Nowadays, the Finite Element Method (FEM) is a powerful numerical method in mechanical computation problems. This method has been successful in many mechanical areas with both academic and industrial applications. Since the FEM is a mesh-based method, it has some drawbacks. For instance, in the large deformation problems which are caused due to distortion elements and may have a negative effect on accuracy, the extraordinary mesh distortion decreases the FEM accuracy and the FEM solution stability [1]. In order to reduce FEM drawbacks, Meshless Methods (MMs) were born to eliminate part of the difficulties associated with dependency on a mesh to construct the approximation field variable [2]. In recent decades, the Functionally Graded Piezoelectric (FGP) structures have been used in various engineering applications due to their inherent electro-mechanical coupling, such as automotive actuators, sensors, and transducers [3-6]. FGPM plates' thermo-electro-mechanical properties vary smoothly through the thickness [7].

Many studies have presented new works on the analysis of the intelligent materials under mechanical, electrical, and thermal loadings using meshless methods. Qirong et al. [8] analyzed simply supported piezoelectric beam under uniformly load distribution using a closed-form solution. Also, some researchers have used closed-form solutions in the past years [9, 10].

Ferreira et al. [11] presented the static behavior of FGM plates using the collocation method by employing radial basis functions. They used third-order shear deformation theory to simulate the plate's kinetic. By using the Timoshenko beam theory, Yang and Xiang [12] studied static and free vibration of the FGPM plate under thermos-electro-mechanical loadings. In their study, the influence of boundary conditions, power law index, and thermal loading on the behavior of the FGPM plate was studied. Chen et al. [13] analyzed buckling of piezoelectric FGM plates by using the Element Free Galerkin (EFG) method. They assumed that applied heat and voltage distribution are non-uniform. Yan et al. [14] analyzed the curved FGP plate by using Airy stress function under electro-thermal loadings. Komeili et al. [15] studied the static bending of FGPM beams under combined thermo-electro-mechanical loading. They compared the accuracy and the reliability of each Euler Bernoulli Theory (EBT), First-order Shear Deformation Theory (FSDT) and Third-order Shear Deformation Theory (TSDT). Singh and Shukla [16] presented nonlinear bending response of FGM plates under various lateral loadings. They used a multi-quadric radial basis function method to approximate field variables. Staňák et al. [17] presented the application of the patch test for Meshless Local Petrov Galerkin (MLPG) analysis of the FGPM circular plate. They used a patch test to address the converge of the MLPG method. Sladek et al. [18] analyzed the bending behavior of a functionally graded piezoelectric circular plate based on the local Petrov-Galerkin method. They assumed material properties are varying along with the plate thickness continuously. They considered mechanical and thermal loads with stationary and transient dynamic conditions. Zhu et al. [19] presented the nonlinear behavior of FGM plates in thermal environments. They used moving Kriging interpolation to develop a local Petrov–Galerkin method. Sator et al. [20, 21] investigated the static response of thin and thick FGM plates using a meshless method. They used a strong formulation to drive governing equations and boundary conditions. To obtain governing equations and boundary conditions at nodal points, they used a Meshless Approximation Method (MLS method) for primary field variables. Meshless method based on the local Petrov-Galerkin approach was utilized for the bending of cylindrical piezoelectric plates under electro-mechanical loading by Staňák et al. [22]. They constructed local integral equations from the weak form of governing PDEs that were defined over local subdomains. They used the Moving Least Squares (MLS) approximation scheme to approximate field variables, and used the Heaviside unit step function as a test function. They also analyzed FGPM using the same method [23]. Li et al. [24] presented the static analysis of piezoelectric structures using a radial basis function on partition of unity method. They derived system equations of the RBF-PUM using the variational principle. As this method possesed delta function property, the boundary conditions can be implemented easily. Three-dimensional meshfree analyses of thick FGPM plate using MLS shape functions

was conducted by Mikaeeli and Behjat [25]. Barati and Zenkour [26] studied the vibrational behavior of the FGP plate using refined four-variable plate theory. They investigated the effect of applied voltage, boundary conditions, thermal loading, and power law index on vibrational behavior of the FGP plate. Buckling of FGPM plate based on refined four-variable plate theory was studied by Barati et al. [27]. They used Three-dimensional Element Free Galerkin (EFG) method for static analysis of thick FGPM plate considering material properties of plate varying smoothly through the thickness by an exponential function. The 3D MLS approximation was used to calculate the shape functions of field variables. Phung Van et al. [28] presented a nonlinear transient dynamic analysis of Functionally Graded Carbon Nanotube Reinforced Composite (FG-CNTRC) Nano plates under transverse uniform load in thermal environments using IGA. They considered that material properties varied smoothly through the thickness. Zenkour and Aljadani [29] studied thermo-electrical buckling of the FGPM nanoscale plate using Eringen's nonlocal elasticity theory. They used Navier's procedure to obtain the exact solution. The effect of nanoscale, thermal loading, power law index, and applying voltage on the buckling value were investigated. Zhang et al. [30] presented a new model for the geometrically nonlinear analysis of FG composite plates with piezoelectric layers. They used the eight-node quadrilateral plate element based on FSDT for nonlinear static and dynamic analyses.

Although lots of studies have been conducted on FGPM plates, most of them have disregarded the effect of power law index together with various coupled electrical, mechanical, and thermal loadings and boundary conditions. Also, there are only a few papers that have analyzed thermo-electro-mechanical behavior of the FGPM plate using meshfree methods. Therefore, one of the novelties of this paper is the analysis of a Functionally Graded Piezoelectric Material (FGPM) plate using meshfree method based on RPIM under thermos-electro-mechanical loadings. A second novelty is the study of the effect of boundary condition and thermos-electro-mechanical loadings on the optimum point of the FGPM plate versus power law index. The effect of different electrical, mechanical, and thermal loading, thickness and boundary conditions on the deflection of the plate is investigated in various power law indices. It is shown that the maximum deflection of the plate with different boundary conditions and electro-thermal loadings is observed in a specific power law index, and thus the proper value for this index can be selected to optimize the overall behavior of the smart structure. In other words,via using these optimum points, it can design sensors and actuators efficiently. Also, by using the RPIM method, the stresses can be obtained in this paper in a simple manner.

2. Theoretical Formulation

2.1. Formulation Using Radial-polynomial Basis

A support domain that has a set of arbitrarily distributed nodes is considered (Fig. 1).

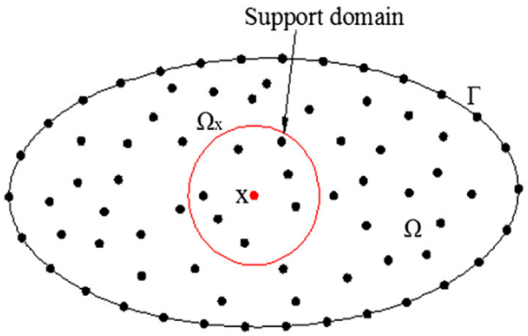

Fig. 1. Domain representation and support domain of 2D model [31].

The approximate function $u^h(x)$ can be estimated to all values of nodes within the support domain based on Radial Point Interpolation Method (RPIM) using radial basis function $R_i(x)$ and polynomial basis function $p_j(x)$ [32]. Evaluated nodal value at interest node x_i at the support domain can be expressed as [31]:

$$u^h(x) = \sum_{i=1}^{n_s} R_i(x)a_i + \sum_{j=1}^{m} p_j(x)b_j = \vec{\mathbf{R}}^{\mathbf{T}}(\mathbf{x})\vec{\mathbf{a}} + \vec{\mathbf{p}}^{\mathbf{T}}(\mathbf{x})\vec{\mathbf{b}} \tag{1}$$

In which, a_i is the unknown coefficients of basis $R_i(x)$, and b_j is the unknown coefficients of polynomial basis p_j.

The number of radial basis n_s is equal to the number of nodes in the supporting domain, and the number of polynomial basis m is chosen according to the problem's conditions [33].

Vector of radial basis "$\mathbf{R}$" and polynomial basis "p" are defined as:

$$\vec{\mathbf{R}}^{\mathbf{T}}(x) = \{R_1(x), R_2(x), \cdots, R_{n_s}(x)\}$$
$$\vec{\mathbf{p}}^{\mathbf{T}} = \{p_1(x), p_2(x), \cdots, p_m(x)\} \tag{2}$$

Unknown coefficients a_i, b_j are estimated by interpolating all points on the supporting domain. Interpolate function of k is defined as:

$$u_k = u(x_k, y_k) \tag{3}$$
$$= \sum_{i=1}^{n_s} a_i R_i(x_k, y_k) + \sum_{j=1}^{m} b_j p_j(x_k, y_k) \quad k = 1, 2, \cdots, n_s$$

Or in matrix form:

$$\vec{\mathbf{U}}_{\mathbf{s}} = \mathbf{R}_{\mathbf{Q}}(\mathbf{x})\vec{\mathbf{a}} + \mathbf{P}_{\mathbf{M}}(\mathbf{x})\vec{\mathbf{b}} \tag{4}$$

in which, $\mathbf{U_s}$ is a vector that contains all field variables of the supporting domain.

In the above equation, the number of unknowns is $n_s + m$. For uniqueness reasons, polynomial basis results should satisfy the following condition [34]:

$$\sum_{i=1}^{n_s} p_j(x_i, y_i) a_i = 0 \qquad j = 1, 2, \cdots, m \tag{5}$$

where Eq. (5) is a homogenous equation. By combining Eq. (4) with Eq. (5), we have:

$$\begin{bmatrix} \mathbf{R_Q} & \mathbf{P_m} \\ \mathbf{P_m^T} & \mathbf{0} \end{bmatrix} \begin{Bmatrix} \vec{\mathbf{a}} \\ \vec{\mathbf{b}} \end{Bmatrix} = \begin{Bmatrix} \vec{\mathbf{U}}_\mathbf{s} \\ \mathbf{0} \end{Bmatrix} \tag{6}$$

Or

$$\mathbf{G} \begin{Bmatrix} \vec{\mathbf{a}} \\ \vec{\mathbf{b}} \end{Bmatrix} = \begin{Bmatrix} \vec{\mathbf{U}}_\mathbf{s} \\ \mathbf{0} \end{Bmatrix} \tag{7}$$

in which moment matrix "$\mathbf{R_Q}$" that forms radial basis is defined as:

$$\mathbf{R_Q} = \begin{Bmatrix} R_1(r_1) & R_2(r_1) & \cdots & R_n(r_1) \\ R_1(r_2) & R_2(r_2) & \cdots & R_n(r_2) \\ \vdots & \vdots & \ddots & \vdots \\ R_1(r_n) & R_2(r_n) & \cdots & R_n(r_n) \end{Bmatrix} \tag{8}$$

where

$$r_k = \left[(x_k - x_i)^2 + (y_k - y_i)^2\right]^{\frac{1}{2}} \tag{9}$$

Moment matrix P_m is a $n_s \times m$ matrix and can be defined as:

$$\mathbf{P}_m = \begin{Bmatrix} P_1(x_1, y_1) & P_2(x_2, y_2) & \cdots & P_m(x_1, y_1) \\ P_1(x_2, y_2) & P_2(x_2, y_2) & \cdots & P_m(x_2, y_2) \\ \vdots & \vdots & \ddots & \vdots \\ P_1(x_n, y_n) & P_2(x_n, y_n) & \cdots & P_m(x_n, y_n) \end{Bmatrix}_{n_s \times m} \tag{10}$$

Since $\mathbf{R_Q}$ is symmetric, the matrix $\mathbf{G}$ is symmetric, too. If the inverse of matrix $\mathbf{G}$ is available, the unique answer of unknown coefficients $\mathbf{a}$, $\mathbf{b}$ can be obtained by multiplying that by the vector of variables.

$$\begin{Bmatrix} \vec{\mathbf{a}} \\ \vec{\mathbf{b}} \end{Bmatrix} = \mathbf{G}^{-1} \begin{Bmatrix} \vec{\mathbf{U}}_\mathbf{s} \\ \mathbf{0} \end{Bmatrix} \tag{11}$$

According to Eq. (5) and Eq. (6), the coefficient is obtained as:

$$\vec{\mathbf{a}} = \mathbf{R_Q^{-1}} \vec{\mathbf{U}}_\mathbf{s} - \mathbf{R_Q^{-1}} \mathbf{P_m} \vec{\mathbf{b}} \tag{12}$$

By substituting Eq. (12) with Eq. (5), the following equation is obtained:

$$\begin{aligned} \vec{\mathbf{b}} &= \mathbf{S_b} \vec{\mathbf{U}}_\mathbf{s} \\ \mathbf{S_b} &= \left[\mathbf{P_m^T R_Q^{-1} P_m}\right]^{-1} \mathbf{P_m^T R_Q^{-1}} \end{aligned} \tag{13}$$

By substituting Eq. (13) with Eq. (12), the unknown coefficient is obtained:

$$\begin{aligned} \vec{\mathbf{a}} &= \mathbf{S_a} \vec{\mathbf{U}}_\mathbf{s} \\ \mathbf{S_a} &= \mathbf{R_Q^{-1}} \left[1 - \mathbf{P_m S_b}\right] = \mathbf{R_Q^{-1}} - \mathbf{R_Q^{-1} P_m S_b} \end{aligned} \tag{14}$$

Finally, Eq. (1) is obtained as:

$$u(x) = \left[\vec{\mathbf{R}}^\mathbf{T}(\mathbf{x}) \mathbf{S_a} + \vec{\mathbf{p}}^\mathbf{T}(x) \mathbf{S_b}\right] \vec{\mathbf{U}}_\mathbf{s} = \vec{\mathbf{\Phi}}(\mathbf{x}) \vec{\mathbf{U}}_\mathbf{s} \tag{15}$$

In which, $\mathbf{\Phi}$ is a shape function matrix that contains n shape functions:

$$\begin{aligned} \vec{\mathbf{\Phi}}(\mathbf{x}) &= \left[\vec{\mathbf{R}}^\mathbf{T}(\mathbf{x}) \mathbf{S_a} + \vec{\mathbf{p}}^\mathbf{T}(x) \mathbf{S_b}\right] \\ &= \left[\phi_1(x), \phi_2(x), \cdots, \phi_i(x), \cdots, \phi_{n_s}(x)\right] \end{aligned} \tag{16}$$

In this paper, MQ radial basis has been used to construct the shape functions:

$$\begin{aligned} R_i(x, y) &= (r_i^2 + C_d^2)^q \\ &= \left[(x - x_i)^2 + (y - y_i)^2 + C_d^2\right]^q \quad (MQ) \end{aligned} \tag{17}$$

where q and C_d are shape parameters which are selected by the user. C_d depends on spacing between the nodes and can be explained as:

$$C_d = \alpha_c \sqrt{\left(\frac{L_x}{nx}\right)^2 + \left(\frac{L_y}{ny}\right)^2} \tag{18}$$

where L_x and L_y are the length and width of plate, respectively. nx and ny are the number of nodes in the sides of the plate along the x and y direction , respectively. α_c is a constant that controls the value of C_d. In this paper, q and α_c have been considered "1.03" and "2", respectively.

2.2. Functionally Graded Piezoelectric Plates

There are various methods for modeling functionally graded materials. In this paper, a simple power law method was used for the modeling problems. In this method, the volume fraction of material was used as following to illustrate the properties of model [35-37]:

$$V_c + V_m = 1 \tag{19}$$

in which, V_c and V_m are the volume fractions of top surface material and bottom surface material. By using power law modeling, we have:

$$V_c = \left(\frac{z}{h} + \frac{1}{2}\right)^n, \quad n \geq 0, \quad -\frac{h}{2} \leq z \leq \frac{h}{2} \tag{20}$$

in which, n is power law index and h is thickness of the plate.

2.2.1. Constitutive Equations of Piezoelectric

The constitutive equation of a piezoelectric material that was obtained from linear thermo-piezoelectricity theory can be expressed as [38]:

$$\begin{aligned} \sigma_{ij} &= C_{ijkl}\varepsilon_{kl} - e_{ijk}E_k - \lambda_{ij}\theta \\ D_l &= e_{lij}\varepsilon_{ij} + k_{lk}E_k + p_l\theta \end{aligned} \tag{21}$$

where σ_{ij} and ε_{kl} are tensors of stress and strain, E_k is electrical field vector, D_l is electrical displacement vector, C_{ijkl} is elasticity tensor, e_{lij} is piezoelectric constant tensor, θ is temperature difference, p_l is pyroelectric vector and k_{lk} is dielectric permittivity coefficient tensor. Thermal expansion tensor can be written as:

$$\lambda_{ij} = C_{ijkl}\alpha_{kl} \tag{22}$$

in which, α_{kl} is thermal expansion coefficient tensor.

2.2.2. Displacements and Strains

Based on the First-order Shear Deformation Theory (FSDT), the displacement field of an arbitrary point in the plate can be expressed as [39]:

$$\begin{aligned} u(x,y,z) &= u_0(x,y) + z\beta_x(x,y) \\ v(x,y,z) &= \nu_0(x,y) + z\beta_y(x,y) \\ w(x,y,z) &= w_0(x,y) \end{aligned} \tag{23}$$

where, the variables u, v and w are displacement of any point of plate and u_0, v_0, w_0 are displacement of midplane of plate and β_x and β_y are rotation of transverse normal about y-axis and x-axis, respectively.
The strains based on the displacements field in Eq. (24) are given by:

$$\begin{aligned} \varepsilon_x &= \frac{\partial u_0}{\partial x} + z\frac{\partial \beta_x}{\partial x}, \quad \varepsilon_y = \frac{\partial v_0}{\partial y} + z\frac{\partial \beta_y}{\partial y} \\ \gamma_{yz} &= \frac{\partial w_0}{\partial y} + \beta_y, \quad \gamma_{xz} = \frac{\partial w_0}{\partial x} + \beta_x \\ \gamma_{xy} &= \frac{\partial u_0}{\partial y} + \frac{\partial v_0}{\partial x} + z\left(\frac{\partial \beta_x}{\partial y} + \frac{\partial \beta_y}{\partial x}\right) \end{aligned} \tag{24}$$

The electric field is defined as the following equation:

$$\left[\vec{E}\right] = \begin{bmatrix} -\dfrac{\partial \varphi}{\partial x} \\ -\dfrac{\partial \varphi}{\partial y} \\ -\dfrac{\partial \varphi}{\partial y} \end{bmatrix} = \left[\vec{R}_\varphi\right]\{\varphi\} \tag{25}$$

in which, R_ϕ is the electric field operator and $\vec{E}$ is the electrical field. In this paper, it is assumed that the electric field has a constant value along the thickness [15, 40-43], and therefore this quantity can be defined as:

$$E_z = -\frac{\varphi}{h_p}, \quad E_x = E_y = 0 \tag{26}$$

where, φ and h_p are the electric potential and the thickness of the piezoelectric layer, respectively.

In this paper, it is assumed that the electric potential has a constant value along the thickness. Equilibrium equation of the plate is derived by using conservation law of momentum and electric charge [44]:

$$\begin{aligned} \delta u^T \psi_u &= -\int_v [\delta\varepsilon]^T[\sigma]dv + \int_v \delta\vec{u}^T\vec{b}dv \\ &\quad + \int_{\Gamma_q} \delta\vec{u}^T\vec{\tau}d\Gamma = 0 \\ \delta\varphi^T\psi_e &= -\int_v \delta E^T D dv + \int_{\Gamma_q} \delta\varphi^T q d\Gamma = 0 \end{aligned} \tag{27}$$

In which, ψ_u and ψ_e are differences between internal and external forces and charges respectively, $\vec{\tau}$ and $\vec{b}$ are surface tractions on the surface Γ_q and body forces, q is the applied electrical charge and v is the volume of plate. By substituting Eq. (27) into Eq. (24) the variational form of conservation equations are derived as:

$$\begin{aligned} &-\int_{A_0} \left(\delta\vec{\varepsilon}_a^T\left[C_s\right]\vec{\varepsilon}_a + \delta\vec{\varepsilon}_b^T\left[E_{e\theta}\right]\varepsilon_{e\theta}\right)dA \\ &+\int_{A_0} \left(\delta u^T b^T + \delta\beta^T b^T\right)dA + \int_{\Gamma_\tau} \delta\bar{u}^T\bar{\tau}d\tau = 0 \\ &-\int_{A_0} \left(\delta E\left[E_G\right]\vec{\varepsilon}_b + \delta E\left[G_E\right]\varepsilon_{e\theta}\right)dA \\ &+\int_{\Gamma_q} \delta\bar{\varphi}\bar{q}d\Gamma = 0 \end{aligned} \tag{28}$$

in which, $\vec{\varepsilon}_a$, $\vec{\varepsilon}_b$, $\varepsilon_{e\theta}$, C_s, $E_{e\theta}$, E_G are described as follows:

$$\begin{aligned} \vec{\varepsilon}_a &= \begin{bmatrix} \varepsilon^0 \\ k^0 \\ \varepsilon_s^0 \end{bmatrix}, \quad \vec{\varepsilon}_b = \begin{bmatrix} \delta\varepsilon^0 \\ \delta K^0 \end{bmatrix}, \quad \varepsilon_{e\theta} = \begin{bmatrix} E \\ \theta \end{bmatrix} \\ G_E &= \begin{bmatrix} [Q] & 0 \\ 0 & [T] \end{bmatrix} \\ E_G &= \begin{bmatrix} [\vec{E}] & 0 \\ 0 & [\hat{E}] \end{bmatrix} \\ E_G &= \begin{bmatrix} [\vec{E}] & -[\bar{\Theta}] \\ [\hat{E}] & -[\hat{\Theta}] \end{bmatrix} \\ [C_s] &= \begin{bmatrix} [A] & [B] & 0 \\ [B] & [D] & 0 \\ 0 & 0 & [A_s] \end{bmatrix} \end{aligned} \tag{29}$$

where $[A]$, $[B]$, and $[D]$ are extensional, bending-extensional coupling, and bending stiffness matrices, respectively and $[\bar{E}]$, $[\hat{E}]$, $[\bar{\Theta}]$, $[\hat{\Theta}]$, $[T]$, and $[Q]$ can be defined as:

$$\begin{aligned}
&[A]=\int_{-\frac{h}{2}}^{\frac{h}{2}}[C]dz, \qquad [B]=\int_{-\frac{h}{2}}^{\frac{h}{2}}z[C]dz,\\
&[D]=\int_{-\frac{h}{2}}^{\frac{h}{2}}z^2[C]dz \quad [\bar{E}]=\int_{-\frac{h}{2}}^{\frac{h}{2}}[\bar{e}]dz,\\
&[\hat{E}]=\int_{-\frac{h}{2}}^{\frac{h}{2}}z[\bar{e}]dz, \qquad [\bar{\Theta}]=\int_{-\frac{h}{2}}^{\frac{h}{2}}[\bar{\lambda}]dz,\\
&[\hat{\Theta}]=\int_{-\frac{h}{2}}^{\frac{h}{2}}z[\bar{\lambda}]dz, \qquad [Q]=\int_{-\frac{h}{2}}^{\frac{h}{2}}[\bar{\varepsilon}]dz,\\
&[T]=\int_{-\frac{h}{2}}^{\frac{h}{2}}[\bar{p}]dz
\end{aligned} \tag{30}$$

2.3. RPIM Modeling

Using RPIM shape functions, the field variables in the support domain can be defined by the following equations:

$$\begin{aligned}
u_0(x,y)&=\sum_{i=1}^{n}\phi_i(x,y)u_{0i}\\
v_0(x,y)&=\sum_{i=1}^{n}\phi_i(x,y)v_{0i}\\
w_0(x,y)&=\sum_{i=1}^{n}\phi_i(x,y)w_{0i}\\
\beta_x(x,y)&=\sum_{i=1}^{n}\phi_i(x,y)\beta_{xi}\\
\beta_y(x,y)&=\sum_{i=1}^{n}\phi_i(x,y)\beta_{yi}\\
\varphi(x,y)&=\sum_{i=1}^{n}\phi_i(x,y)\varphi_i
\end{aligned} \tag{31}$$

where, ϕ_i is the shape function, $u, v, w, \beta_x, \beta_y, \varphi$ are the nodal values of displacements, rotations and electric potential in the plate, and n is the number of nodes in the support domain. In addition, temperature in the element field is described as follows:

$$\theta(x,y)=\sum_{i=1}^{n}\phi_i(x,y)\theta_i \tag{32}$$

where, θ_i is the nodal value of temperature in the plate.

Also, strain-displacement relations in matrix form can be written as:

$$\begin{aligned}
[\varepsilon]&=[B_u]\{u\}\\
&=[R_a]\{u\}+z[R_b]\{u\}+[R_s]\{u\}
\end{aligned} \tag{33}$$

where, $[R_a]$, $[R_b]$, $[R_s]$ are strain operators based on the displacements-strain relations and can be defined as follows:

$$[R_a]=\begin{bmatrix}
\frac{\partial\phi_i}{\partial x} & 0 & 0 & 0 & 0\\
0 & \frac{\partial\phi_i}{\partial y} & 0 & 0 & 0\\
\frac{\partial\phi_i}{\partial y} & \frac{\partial\phi_i}{\partial x} & 0 & 0 & 0
\end{bmatrix}$$

$$[R_b]=\begin{bmatrix}
0 & 0 & 0 & \frac{\partial\phi_i}{\partial x} & 0\\
0 & 0 & 0 & 0 & \frac{\partial\phi_i}{\partial y}\\
0 & 0 & 0 & \frac{\partial\phi_i}{\partial y} & \frac{\partial\phi_i}{\partial x}
\end{bmatrix} \tag{34}$$

$$[R_s]=\begin{bmatrix}
0 & 0 & \frac{\partial\phi_i}{\partial x} & 1 & 0\\
0 & 0 & \frac{\partial\phi_i}{\partial y} & 0 & 1
\end{bmatrix}$$

Combining Eq. (33) with Eq. (28), and integrating through A_0, the final equation of motion of plate in the matrix form can be obtained as:

$$[K_{dd}][\vec{U}]+[K_{de}][\vec{\varphi}^s]+[K_{de}][\vec{\varphi}^a]-[K_{d\theta}][\vec{\theta}]=[F] \tag{35}$$

$$[K_{ed}][\vec{U}]-[K_{ee}][\vec{\varphi}^s]-[K_{ee}][\vec{\varphi}^a]+[K_{d\theta}][\vec{\theta}]=0 \tag{36}$$

where submatrices K_{dd}, K_{de} and K_{ee} indicate the elastic, piezoelectric, and permittivity stiffness matrices; and $K_{d\theta}$ and $K_{e\theta}$ are the coupled thermal expansion and pyroelectric stiffness matrices of the structure. These matrices are expressed as:

$$\begin{aligned}
[K_{dd}]=\iint_{A_e}\big(&[R_a]^T[A][R_a]+[R_a]^T[B][R_a]\\
&+[R_b]^T[B][R_a]+[R_b]^T[D][R_b]\\
&+[R_s]^T[A_s][R_s]\big)|J|dA
\end{aligned} \tag{37}$$

$$[K_{de}]=\iint_{A_e}\big([R_a]^T[\bar{E}][R_\varphi]+[R_b]^T[E][R_\varphi]\big)|J|dA$$

$$[K_{ee}]=\iint_{A_e}\big([R_\varphi]^T[G][R_\varphi]\big)|J|dA$$

$$[K_{d\theta}]=\iint_{A_e}\big([R_a]^T[\bar{\Theta}][R_\theta]+[R_b]^T[\hat{\Theta}][R_\theta]\big)|J|dA$$

The five degrees of freedom including displacements and rotations were collected in nodal vector $\vec{U}$. φ, θ are

the electric potential and applied temperature nodal vectors, respectively. $|J|$ is the Jacobian determinant for numerical integration. To identify the sensory and actuator voltage, s and a superscripts were used, respectively.

By substituting electric potential in Eq. (35) to Eq. (36), the final equation of the plate can be obtained as:

$$\begin{aligned}&\big([K_{dd}]+[K_{de}][K_{ee}]^{-1}[K_{ed}]\big)[\vec{U}]=\\&[F]+[K_{d\theta}][\vec{\theta}]-[K_{de}][K_{ee}]^{-1}[K_{e\theta}][\vec{\theta}]\\&+[K_{de}][K_{ee}]^{-1}[K_{ee}][\vec{\varphi}^{a}]-[K_{de}][\vec{\varphi}^{a}]\end{aligned}\tag{38}$$

As mentioned above, the radial point interpolation method is used in this article to model the plate. In this paper, each node has 6 degrees of freedom: three displacements (u, v, w), two rotations (β_x, β_y), and one electric potential "φ". To model the FGPM plate, 15×15 nodes are distributed within the domain, and thus the domain contains 225 nodes. This selection is based on the convergence study of the plate response. By using the conservation of momentum and electric charge laws, the stiffness matrices are obtained. The RPIM shape function satisfies Kronecker delta condition. Therefore, it can apply boundary conditions to stiffness and force matrices directly as the finite element method does. By applying boundary conditions, the final set of equations for the solution is obtained.

3. Results

This study conducted a bending analysis of the FGPM plate under mechanical and electrical loadings by dimensions of $50.8 \times 50.8\text{mm}^2$ (Fig. 2) . The plate consists of FGMs in which the top surface of the plate is (Poly Vinylidene Fluoride) (PVDF) rich and bottom surface is PZT rich. The material properties of the plate are listed in Table 1. In addition, for the sake of convenience, in this paper, the clamped boundary condition in the plate is shown by "C", simply supported is shown by "S", and free is shown by "F". Also non-dimensional deflection is $\frac{w_{\max}10^3}{h}$, where $w_{\max}$, and h are maximum deflection and thickness of the FGPM plate, respectively.

As it is known, there is a shear-locking phenomenon in analysis of plates if the width to -thickness ratio $\left(\frac{h}{a}\right)$ of a plate becomes much lower $\frac{h}{a} = 0.02$. To handle shear-locking effect, there are several options. Methods used in FEM can be applied to avoid shear locking in meshfree methods. In addition, we can use high-order basis functions to solve this problem. Using the derivatives of the deflection shape functions as the shape functions for the rotations can eliminate shear locking effect [32]. However, in this paper, a square plate by dimensions with thickness to-width ratio $\frac{h}{a} = 0.06$ is analyzed. According to Liu [32], there is no shear locking, if $\frac{h}{a} > 0.01$, even if m $m = 3$ is used. Therefore, in this paper, shear locking effect will not occur.

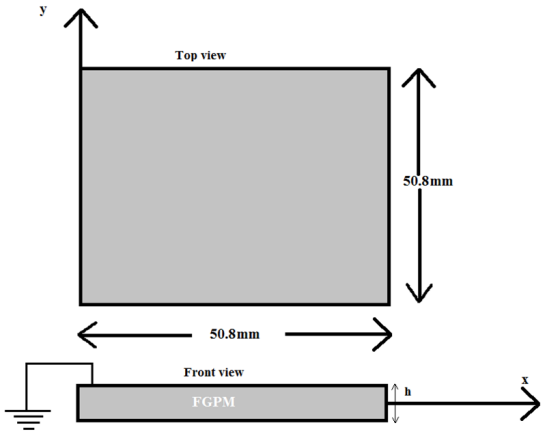

Fig. 2. Geometry of the plate.

3.1. Comparison Study

To ensure the accuracy of the present meshfree RPIM method in this article, a bimorph piezoelectric plate is analyzed.

In this case, one clamped bimorph piezoelectric beam under 1V electrical loading by dimensions of $100 \times 5 \times 1\text{mm}^3$ is statically analyzed, and the results are compared with Cen et al.'s [45]. Fig. 3 shows the dimensionless centerline deflection of the plate. It is observed that the present RPIM method's results have good agreement with Cen et al.'s [45] study.

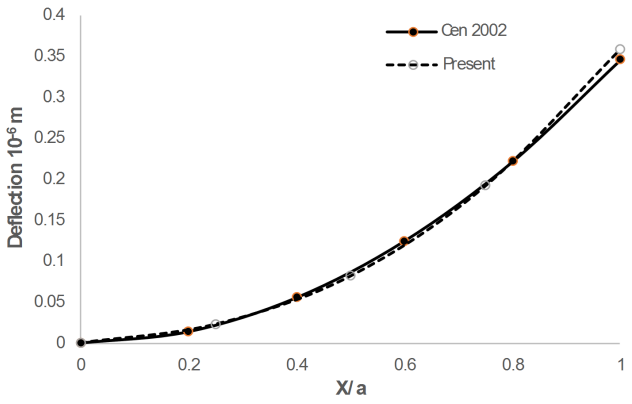

Fig. 3. Tip deflection of the bimorph beam and comparison.

In addition, to assure the accuracy of the results, the convergence study of results is conducted in this section. The convergence of the maximum deflection of square FGPM plate with three types of boundary conditions under uniform mechanical loading is carried out (Fig. 4). It is observed that by using 15×15 node numbers, the results can reach good convergence.

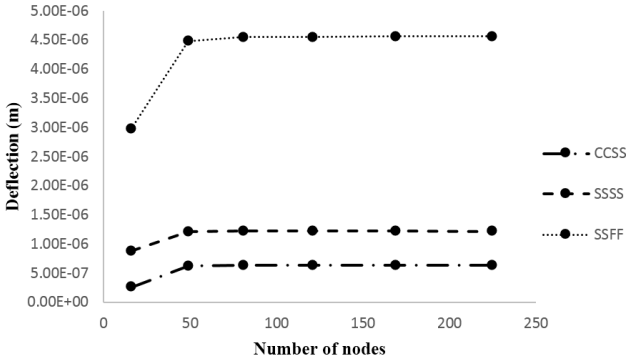

Fig. 4. Convergence study of RPIM method for different boundary conditions.

3.2. Thermal Loading

In this section, the deflection and stresses of the FGPM plate in different boundary conditions, under thermal loading are investigated. Fig. 5 shows the maximum deflection of the FGPM plate under $\theta = 50°C$ thermal loading in three boundary conditions: "CCSS", "CFFF", and "SSFF".

It is seen from these figures that the maximum deflection of the FGPM plate occurs in "$n = 0.6$" in thermal loading. It means the FGPM plate has maximum deflection under thermal loading, which can be used for the selection of optimum performance of sensors and actuators in thermal environments. It is also seen that, by increasing power index, the maximum deflection of the plate increases and then decreases. This is due to the difference in thermal expansion coefficients of PZT and PVDF and the interaction between Young's modulus and thermal expansions coefficient of the two materials. This behavior of the FGPM plate occurs regardless of the mentioned boundary conditions.

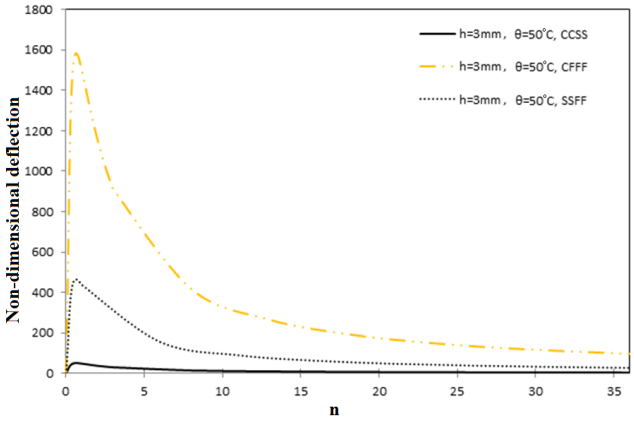

Fig. 5. Maximum deflection of FGPM plate with 3mm thickness versus power law index.

Fig. 6 shows the maximum deflection of FGPM plate for three types of boundary conditions in different thermal loadings. It is seen that, by increasing thermal load, the maximum deflection of the plate increases until "$n = 0.6$" and then decreases. Therefore this value can be the optimum power index for all thermal loadings.

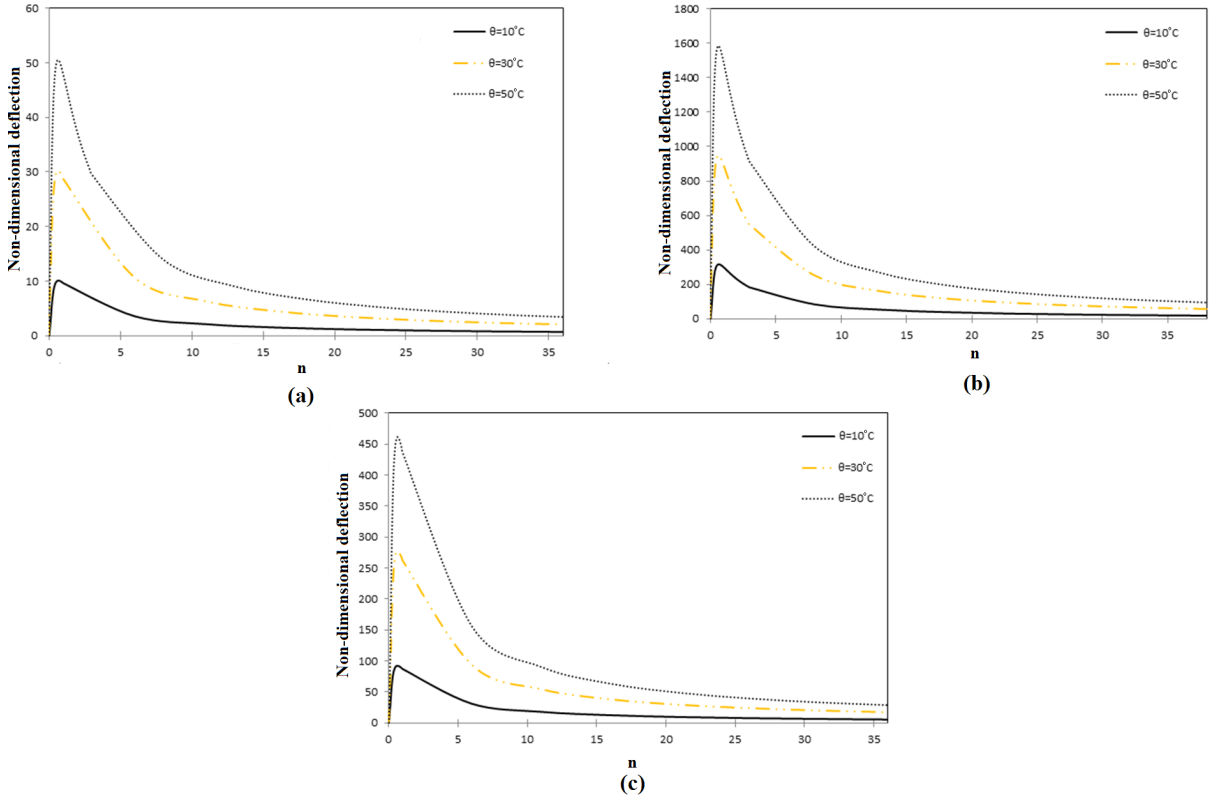

Fig. 6. Maximum deflection of FGPM plate with 3mm thickness subjected to various thermal loads: a) CCSS b) CFFF c) SSFF.

Fig. 7 shows the distribution of normal and shear stresses, σ_{xx}, and σ_{xy}, respectively through the thickness of the plate at the point $\left(\frac{a}{2}, \frac{b}{2}\right)$ under uniform $\theta = 10°C$ thermal loading. It is observed that when plate is homogeneous ($n = 0$), the normal stress σ_{xx} is constant through the thickness. When ($n = 0$), the matrix $[\hat{\Theta}] = 0$, and therefore there is no deflection, and normal stresses will be constant through the thickness. Increasing power law index value changes the distribution of normal stress changes. It is seen that the manner of stress distribution depends on the boundary conditions at thermal loadings.

3.3. Electrical Loading

In this section, the effect of electrical load on the deflection and stresses of the FGPM plate is shown, and the static response of the system subjected to electrical loads is investigated. Fig. 8 shows non-dimensional maximum deflection of the FGPM plate under electrical load with different boundary conditions. It is seen that, by increasing the power law index, maximum deflection increases and then decreases. This phenomenon is because of differences between piezoelectric constants of PZT and PVDF and the interaction between piezoelectric constant and Young's modulus of these materials. It is also seen from these figures, the maximum deflection in all cases occurs at power law value of "$n = 0.3$". Fig. 9 illustrates maximum deflection of the centerline of the FGPM plate for different electrical loadings. It is also seen that power index related to maximum deflection of FGPM plate does not change and occurs for all cases in "$n = 0.3$".

Fig. 10 shows the distribution of normal stresses σ_{xx} and shear stresses σ_{xy} through the thickness of the plate at the point $\left(\frac{a}{2}, \frac{b}{2}\right)$ under uniform 80V electrical loading.

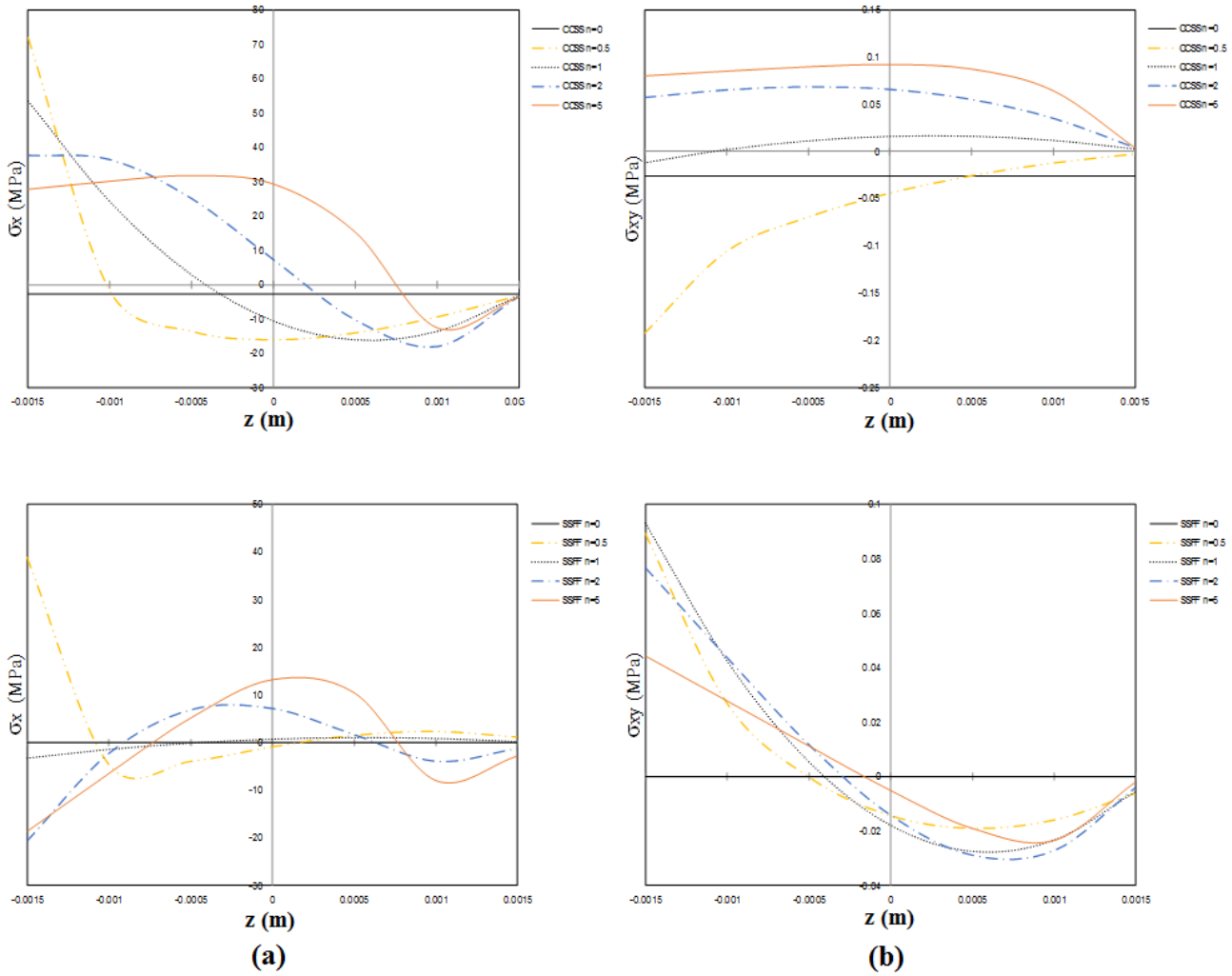

Fig. 7. Normal and shear stresses of FGPM plate with various power index law subjected to $\theta = 10°C$ thermal loading: a) σ_{xx}, b) σ_{xy}.

It is obvious that when a FGPM plate is homogeneous ($n = 0$), the normal stress σ_{xx} is constant through the thickness. When ($n = 0$), the matrix $[\hat{E}]$ is equal to zero, and thus there are constant normal stresses through the thickness. Increasing the power law index value changes the distribution of normal stress. The manner of stress distribution depends on boundary conditions at thermal loadings.

3.4. Combined Electrical and Mechanical Loading

Fig. 11 illustrates the effect of the applied voltage on non-dimensional maximum centerline deflection of the FGPM plate. This plate which has three boundary conditions (CCSS, CFFF, SSFF) is subjected to 1KN/m^2 uniform loading. It is seen that applying the voltage of 80V decreases deflection for lower power index "n", but after about $n = 10$, the effect of applied voltage is not significant. According to these figures, by increasing "n", the deflection of plate decreases given that by increasing n, stiffness of the plate increases. Fig. 11 gives a detailed view of the "SSFF" boundary condition of the FGPM plate up to power law index of "2".

Fig. 12 depicts the through-the-thickness distributions of the normal stresses σ_{xx}, and transverse shear stresses σ_{xz} in the middle point $\left(\frac{a}{2}, \frac{b}{2}\right)$ of the FGPM plate under the uniform mechanical loading. From this figure, it is observed that when "$n = 0$", the normal stress σ_{xx} is linear through the thickness, but by increasing power law index, the distribution of normal stress changes. The maximum compressive stresses under mechanical loadings occur at a point on the top surface, and the maximum tensile stresses occur, at a point on the bottom surface of the FGPM plate.

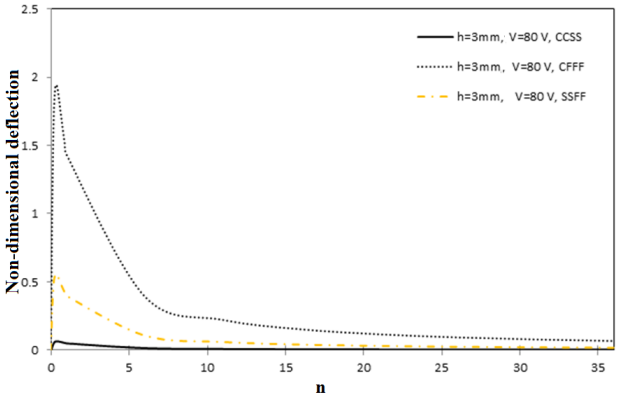

Fig. 8. Centerline deflection of FGPM plate with different boundary conditions subjected to electrical loadings.

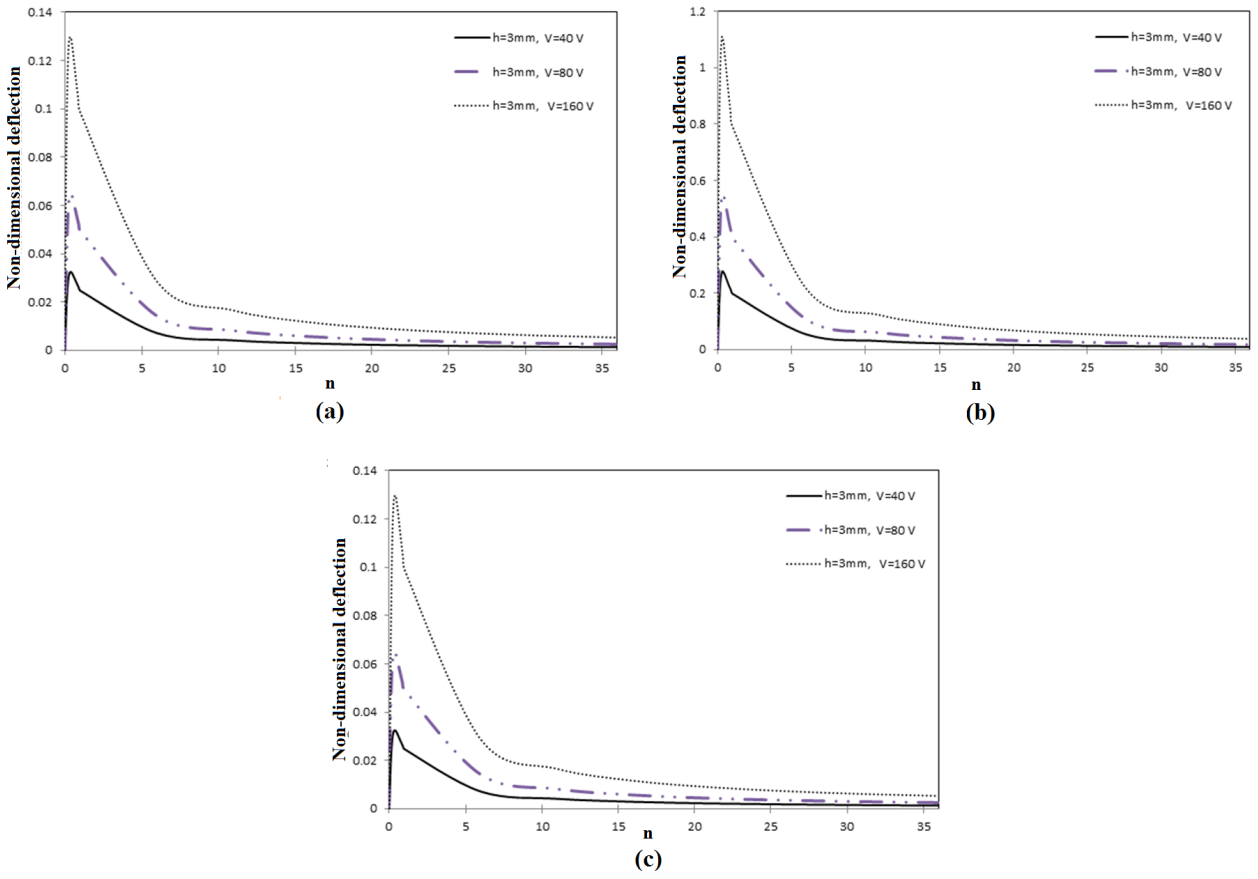

Fig. 9. Centerline deflection of FGPM plate with 3mm thickness subjected to different electrical loads: a) CCSS b) CFFF c) SSFF.

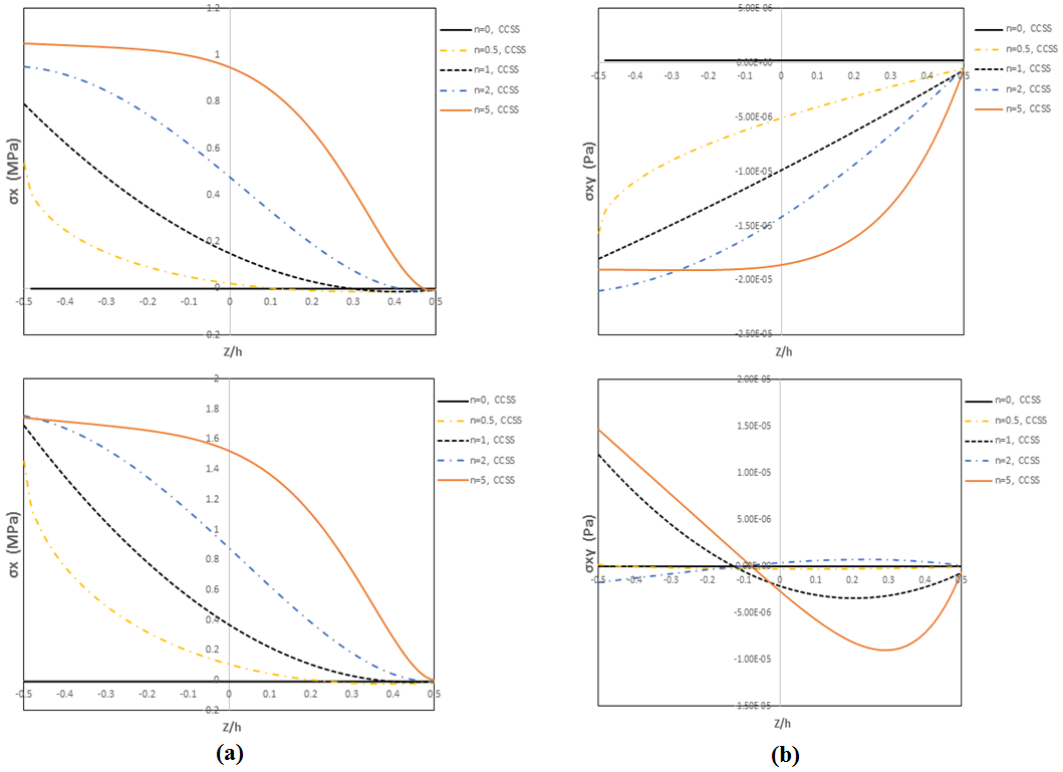

Fig. 10. Normal and shear stresses of FGPM plate with various power index law subjected to 80V electrical loading: a) σ_{xx} b) σ_{xy}.

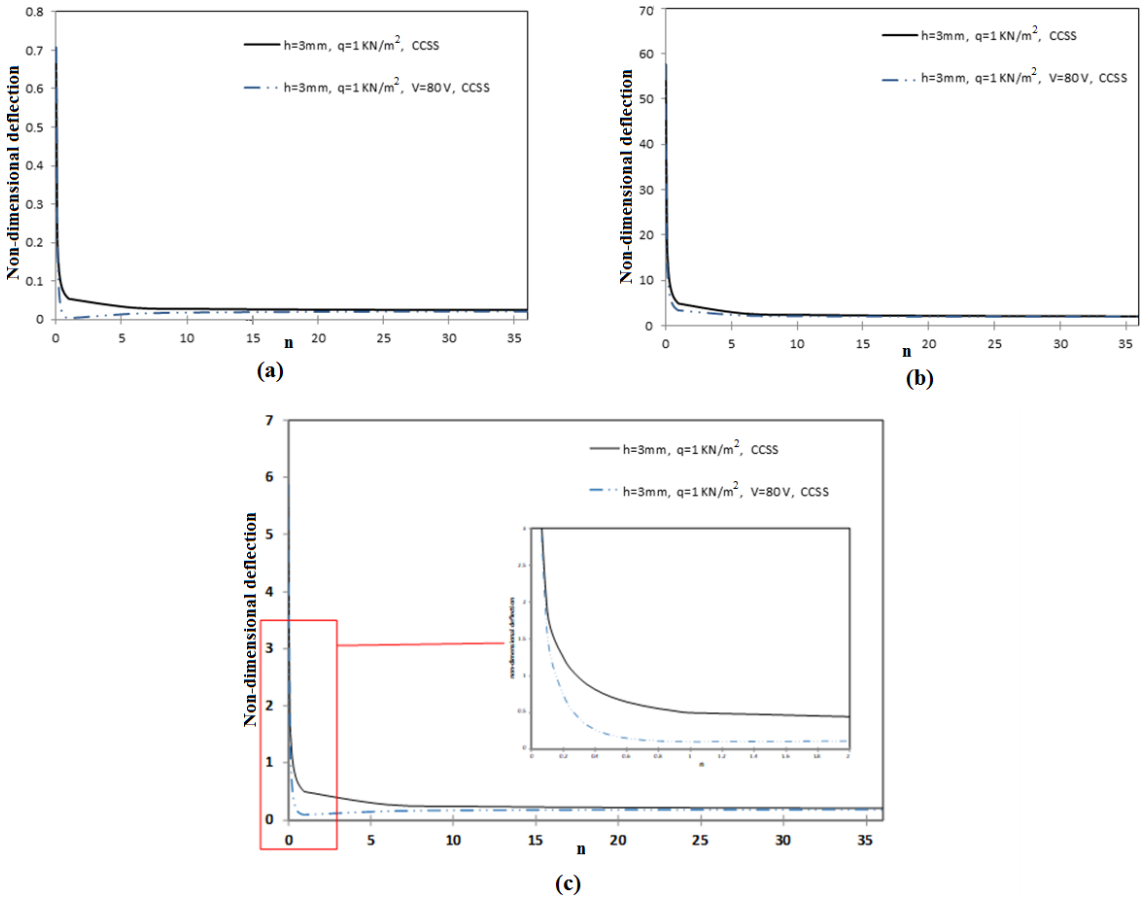

Fig. 11. Centerline deflection of FGPM plate subjected to 1KN/m^2 and 80V load: a) CCSS b) CFFF c) SSFF.

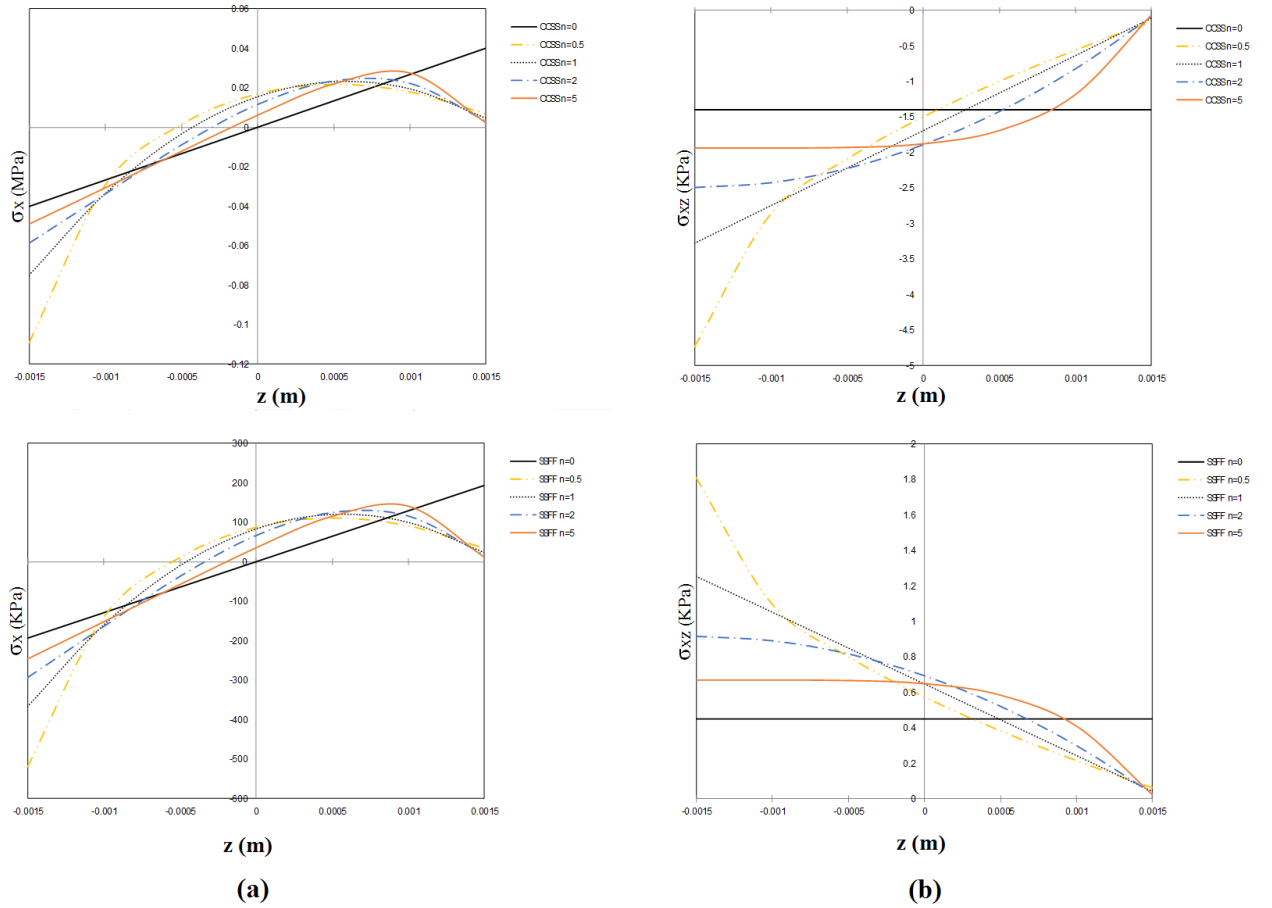

Fig. 12. Normal and transverse stresses of FGPM plate with various power index law subjected to uniform mechanical loading 1kN/m^2: a) σ_{xx} b) σ_{xz}.

4. Conclusions

In this paper, static analysis of FGPM plates are conducted based on FSDT plate theory under mechanical, electrical, and thermal loads using a meshfree method based on the RPI method. Governing equations of the FGPM plate are derived by using equilibrium equations. At first, by performing a comparison study, the accuracy of the present meshfree RPI method is ensured. To reach good converge, 15×15 node numbers, and $q = 1.03$ are used. By using the "MQ" radial basis function and polynomial basis ($m = 3$),the effects of different power indexes, boundary conditions, and thermal, mechanical, and electrical loads on the bending of FGPM are investigated. The RPIM shape function passes the Kronecker delta condition, and thus boundary conditions are applied directly. The stresses are computed in each case study, and it has been shown that stress distribution is nonlinear through the thickness at nonzero index law values. It is seen that, by increasing power law index, in the electro-mechanical loading, the deflection decreases smoothly, but under thermal and electrical loading, the deflection increases at first, and then decrease by increasing power law index. The maximum deflection occurred at $n = 0.6$ and $n = 0.3$ under thermal and electrical loading regardless of boundary conditions (CCSS, CFFF, and SSFF), applying voltage and thermal loading. This property can be used for the selection of optimum performance of sensors and actuators in thermal environments. In this paper, it is shown that RPIM is a proper procedure for analyzing the bending behavior of the FGPM plate under electro-thermal and mechanical loading. It is because RPIM has good convergence rate, and it is easy to implement.

Acknowledgments

This research did not receive any specific grant from funding agencies in the public, commercial, or not-for-profit sectors.

References

[1] J. Belinha, A.L. Araújo, A.J.M. Ferreira, L.M.J.S. Dinis, R.M. Natal Jorge, The analysis of laminated plates using distinct advanced discretization meshless techniques, Compos. Struct., 143 (2016) 165-179.

[2] P. Zhu, K.M. Liew, Free vibration analysis of moderately thick functionally graded plates by local Kriging meshless method, Compos. Struct., 93(11) (2011) 2925-2944.

[3] P.J.C. Branco, J.A. Dente, On the electromechanics of a piezoelectric transducer using a bimorph cantilever undergoing asymmetric sensing and actuation, Smart Mater. Struct., 13(4) (2004) 631-642.

[4] H. Gu, Y. Moslehy, D. Sanders, G. Song, Y.L. Mo, Multi-functional smart aggregate-based structural health monitoring of circular reinforced concrete columns subjected to seismic excitations, Smart Mater. Struct., 19(6) (2010) 065026.

[5] K.M. Liew, X.Q. He, T.Y. Ng, S. Sivashanker, Active control of FGM plates subjected to a temperature gradient: Modelling via finite element method based on FSDT, Int. J. Numer. Methods Eng., 52(11) (2001) 1253-1271.

[6] X. Guo, D. Fang, A.K. Soh, H.C. KIM, J.J. Lee, Analysis of piezoelectric ceramic multilayer actuators based on an electro-mechanical coupled meshless method, Acta Mech. Sin., 22(1) (2006) 34-39.

[7] X.H.Wu, Y.P. Shen, X.G. Tian, A high order theory for functionally graded piezoelectric shells, Int. J. Numer. Methods Eng., 39(20) (2002) 5325-5344.

[8] L. Qirong, L. Zhengxing, J. Zhanli, A close-form solution to simply supported piezoelectric beams under uniform exterior pressure, Appl. Math. Mech., 21(6) (2000) 681-690.

[9] L. Qi-rong, L. Zheng-xing, W. Zong-li, Analysis of beams with piezoelectric actuators, Appl. Math. Mech., 22(9) (2001) 1074-1081.

[10] Z. Lin-nan, S. Zhi-fei, Analytical solution of a simply supported piezoelectric beam subjected to a uniformly distributed loading, Appl. Math. Mech., 24(10) (2003) 1215-1223.

[11] A.J.M. Ferreira, R.C. Batra, C.M.C. Roque, L.F. Qian, P.A.L.S. Martins, Static analysis of functionally graded plates using third-order shear deformation theory and a meshless method, Compos. Struct., 69(4) (2005) 449-457.

[12] J. Yang, H.J. Xiang, Thermo-electro-mechanical characteristics of functionally graded piezoelectric actuators, Smart Mater. Struct., 16(3) (2007) 784-797.

[13] X.L. Chen, Z.Y. Zhao, K.M. Liew, Stability of piezoelectric FGM rectangular plates subjected to non-uniformly distributed load, heat and voltage, Adv. Eng. Software, 39(2) (2008) 121-131.

[14] Z. Yan, M. Zaman, L. Jiang, Thermo-electro-mechanical analysis of a curved functionally graded piezoelectric actuator with sandwich structure, Materials, 4(12) (2011) 2151-2170.

[15] A. Komeili, A.H. Akbarzadeh, A. Doroushi, M.R. Eslami, Static analysis of functionally graded piezoelectric beams under thermo-electro-mechanical loads, Adv. Eng. Software, 3 (2011) 153731.

[16] J. Singh, K.K. Shukla, Nonlinear flexural analysis of functionally graded plates under different loadings using RBF based meshless method, Eng. Anal. Boundary Elem., 36(12) (2012) 1819-1827.

[17] P. Staňák, V. Sládek, J. Sládek, S. Krahuleca, L. Sátor, Application of patch test in meshless analysis of continuously non-homogeneous piezoelectric circular plate, Appl. Comput. Anal., 7(1) (2013) 65-76.

[18] J. Sládek, V. Sládek„ P. Stanak, C. Zhang, M. Wünsche, Analysis of the bending of circular piezoelectric plates with functionally graded material properties by a MLPG method, Eng. Struct., 47 (2013) 81-89.

[19] P. Zhu, L.W. Zhang, K.M. Liew, Geometrically nonlinear thermomechanical analysis of moderately thick functionally graded plates using a local Petrov–Galerkin approach with moving Kriging interpolation, Compos. Struct., 107 (2014) 298-314.

[20] L. Sator, V. Sladek, J. Sladek, Coupling effects in elastic analysis of FGM composite plates by meshfree methods, Compos. Struct., 115 (2014) 100-110.

[21] L. Sator, J. Sládek, V. Sládek, D.L. Young, Elastodynamics of FGM plates by mesh-free method, Compos. Struct., 140 (2016) 309-322.

[22] P. Staňák, J. Sládek, V. Sládek, S. Krahulec, Numerical MLPG Analysis of Piezoelectric Sensor in Structures, Slovak J. Civ. Eng., 22(2) (2014) 15-20.

[23] P. Stanak, J. Sládek, V. Sládek, A. Tadeu, Three-Dimensional Meshless Modelling of Functionally Graded Piezoelectric Sensor, In: Březina T., Jabloński R. (eds) Mechatronics 2013, Cham: Springer International Publishing, (2014).

[24] S. Li, L. Yao, S. Yi, W. Wang, A meshless radial basis function based on partition of unity method for piezoelectric structures, Math. Prob. Eng., 2016 (2016) 7632176.

[25] S. Mikaeeli, B. Behjat, Three-dimensional analysis of thick functionally graded piezoelectric plate using EFG method, Compos. Struct., 154 (2016) 591-599.

[26] M.R. Barati, A.M. Zenkour, Electro-thermoelastic vibration of plates made of porous functionally graded piezoelectric materials under various boundary conditions, J. Vib. Control, 24(10) (2016) 1910-1926.

[27] M.R. Barati, H. Shahverdi, A.M. Zenkour, Electro-mechanical vibration of smart piezoelectric FG plates with porosities according to a refined four-variable theory, Mech. Adv. Mater. Struct., 24(12) (2017) 987-998.

[28] P. Phung Van, T. Cuong Le, H. Nguyen-Xuan, M. Abdel Wahab, Nonlinear transient isogeometric analysis of FG-CNTRC nanoplates in thermal environments, Compos. Struct., 201 (2018) 882-892.

[29] A.M. Zenkour, M.H. Aljadani, Thermo-electrical buckling response of actuated functionally graded piezoelectric nanoscale plates, Results Phys., 13 (2019) 102192.

[30] S.Q. Zhang, Y.S. Gao, G.Z. Zhao, Y.J. Yu, M.Chen, X.F. Wang, Geometrically nonlinear analysis of CNT-reinforced functionally graded composite plates integrated with piezoelectric layers, Compos. Struct., 234 (2020) 111694.

[31] H.H. Phan-Dao, C.H. Thai, J. Lee, H. Nguyen-Xuan, Analysis of laminated composite and sandwich plate structures using generalized layerwise HSDT and improved meshfree radial point interpolation method, Aerosp. Sci. Technol., 58 (2016) 641-660.

[32] G.R. Liu, Mesh Free Methods: Moving Beyond The Finite Element Method, CRC Press, New York, (2009).

[33] G.R. Liu, Y.T. Gu, An Introduction to Meshfree Methods and Their Programming, Springer, (2005).

[34] M.A. Golberg, C.S. Chen, H. Bowman, Some recent results and proposals for the use of radial basis functions in the BEM, Eng. Anal. Boundary Elem., 23(4) (1999) 285-296.

[35] B. Yildirim, S. Dag, F. Erdogan, Three dimensional fracture analysis of FGM coatings under thermomechanical loading, Int. J. Fract., 132(4) (2005) 371-397.

[36] J. Reddy, Analysis of functionally graded plates, Int. J. Numer. Methods Eng., 47(1-3) (2000) 663-684.

[37] T.Y. Ng, K.Y. Lam, K.M. Liew, J.N. Reddy, Dynamic stability analysis of functionally graded cylindrical shells under periodic axial loading, Int. J. Numer. Methods Eng., 38(8) (2001) 1295-1309.

[38] J. Yang, H.J. Xiang, Thermo-electro-mechanical characteristics of functionally graded piezoelectric actuators, Smart Mater. Struct., 16(3) (2007) 784-797.

[39] J.N. Reddy, On laminated composite plates with integrated sensors and actuators, Eng. Struct., 21(7) (1999) 568-593.

[40] M.H. Babaei, G. Akhras, Graded piezoelectric cylinders subjected to high electric fields and comparison of their frequency response with piezoelectric plates, Meccanica, 49(6) (2014) 1527-1538.

[41] A. Armin, I. Shafieenejad, N. Moallemi, A.B. Novinzadeh, Comparison between hpm and finite fourier solution in static analysis of fgpm beam under thermal load, J. Theor. Appl. Mech., 48(1) (2010) 173-189.

[42] K. Takagi, J.F. Li, S. Yokoyama, R. Watanabe, A. Almajid, M.Taya, Design and fabrication of functionally graded PZT/Pt piezoelectric bimorph actuator, Sci. Technol. Adv. Mater., 3(2) (2002) 217-224.

[43] M. Taya, A.A. Almajid, M. Dunn, H. Takahashi, Design of bimorph piezo-composite actuators with functionally graded microstructure, Sens. Actuators A, 107(3) (2003) 248-260.

[44] D. Varelis, D.A. Saravanos, Non-linear coupled multi-field mechanics and finite element for active multi-stable thermal piezoelectric shells, Int. J. Numer. Methods Eng., 76(1) (2008) 84-107.

[45] S. Cen, A.K. Soh, Y.Q. Long, Z.H.Yao, A new 4-node quadrilateral FE model with variable electrical degrees of freedom for the analysis of piezoelectric laminated composite plates, Compos. Struct., 58(4) (2002) 583-599.